RESEARCH

Experimental Investigation of Cyclic Variation of the In-Cylinder Flow in a Spark-Ignition Engine with a Charge Motion Control Valve

Fuquan Tian[1] · Lei Shi[1] · Zhizhao Che[1] · Zhen Lu[1] · Kai Sun[1] · Tianyou Wang[1]

Abstract

The cycle-to-cycle variations (CCV) have a substantial impact on the improvement of thermal efficiency and the expansion of operational limitations in internal combustion engines. For spark ignition engines, the variation of the in-cylinder flow field, especially the CCV of flow near the spark plug at the ignition timing, is a key factor causing the CCV of combustion. However, the physical mechanisms behind the CCV control of the in-cylinder flow field are still not well understood. The objective of this study is to determine how different tumble intensities induced by manipulating the opening and shutting of a tumble flap influence the flow CCV at the spark plug position at the ignition timing. High-speed particle image velocimetry (PIV) measurements were performed in an optically accessible single-cylinder, spark-ignited engine at a constant engine speed of 800 rpm. The frequency distributions of the velocity magnitude and flow angle are more concentrated under the high tumble intensity, indicating that the CCV of flow at the spark plug position at the ignition timing can be effectively reduced by closing the tumble flap. To gain a deeper insight into the mechanism of flow CCV alleviation, a correlation map analysis was employed, which can determine the relationship between the flow at the spark plug position and the flow distribution during the intake and compression stroke in time and space. To enhance the correlation between the above two, the proper orthogonal decomposition (POD) method was employed to extract the large-scale coherent structures and then the flow fields were reconstructed. The results demonstrated that the factors influencing the flow CCV under the tumble flap opening condition are primarily attributed to the CCV of the collision region position of the two intake jet flows in the later stage of the intake stroke and flow shear with the combustion chamber wall at the late compression stroke, while the factor influencing the flow CCV under the tumble flap closing condition is mostly connected to the CCV of tumble vortex position. Besides, closing the tumble flap can markedly increase the averaged kinetic energy and turbulent kinetic energy of the flow field in the vicinity of the spark plug position in the late compression stroke.

Keywords Cycle-to-cycle variations · Spark ignition engines · In-cylinder flow · Particle image velocimetry · Tumble flap · Factors influencing the CCV

---

1 Introduction

Increasing the thermal efficiency of internal combustion engines (ICEs) has long been a primary concern in the combustion disciplines, especially in the context of the tightening of emission restrictions and the pursuit of low-carbon power in recent years. Many technologies, such as direct injection, turbocharging, cooled exhaust gas recirculation (EGR), and downsizing, have been proven to enhance the thermal efficiency of spark-ignition (SI) engines by overcoming the restrictions of well-mixed stoichiometric operation. However, there are still some limitations on the thermal efficiency of SI engines under stoichiometric operation, the reasons mainly are as follows: (a) the pumping losses caused by the required intake throttling, (b) substantial heat-transfer losses and unfavorable thermodynamic characteristics of the combustion products resulting from the high combustion temperatures, and (c) the stoichiometric combustion failing to finish close to top dead center (TDC) (Jung et al. 2017).

In addition to the several technical routes mentioned above for SI engines, lean burn is widely regarded as an advanced combustion technology to reduce fuel consumption and exhaust emissions and achieve higher thermal efficiency, which can enhance combustion quality, minimize heat transfer losses, and allow for higher compression ratios (Malé et al. 2019; Benoit et al. 2022). Despite its benefits, lean burn technology can only be operated under restricted conditions due to the increase in the cycle-to-cycle variations (CCV) of combustion with the air dilution level. The existence of combustion CCV in SI engines has been observed universally, nevertheless, this issue would be further aggravated under partial loads, low speed, and lean operation conditions. The high combustion CCV levels can deteriorate the engine's operational stabilities, increase fuel consumption and exhaust emissions, and reduce the engine's operating range and power output. It has been estimated that eliminating the combustion CCV might increase power output by around 10% for the same fuel consumption in a SI engine (Ozdor et al. 1994).

The factors inducing the combustion CCV in SI engines have been identified as coming from different aspects, such as the variation of the in-cylinder flow field, the variations in the air–fuel ratio and the EGR, the spatial inhomogeneity of mixture composition particularly close to the spark plug, and the spark discharge characteristics and flame kernel development (Heywood 2018; Pera et al. 2014; Chu et al. 2022). Throughout the working process of the engine, all of these factors strongly interact. There have been many studies on the analysis of combustion CCV in ICEs, and a considerable number of results manifested that the variation in the in-cylinder flow field is a key factor causing the combustion CCV of SI engines (Young 1981; Hinze and Cheng 1998; Goryntsev et al. 2009; Buschbeck et al. 2012; Granet et al. 2012; Welch et al. 2022). After reviewing the literature involving cyclic combustion and pressure-development variations, Young (1981) concluded that CCV in combustion originated in the early stage of the combustion process, and the CCV of velocity in the vicinity of the spark plug at the ignition timing, which has an impact on the developing flame kernel, was assumed to be the primary cause of these variations. Hinze and Cheng (1998) performed a quantitative assessment of the factors that affect the SI engine CCV of combustion at idle operation through a series of charge perturbation experiments, the results indicated the variation in residual gas mass contributes about 1/3 to CCV, the variations in the air and fuel only contribute to 7.5% and 4.6%, respectively, and the remaining 54% is caused by the flow field and charge inhomogeneity variations. By using high-speed PIV in an optically accessible gasoline engine, Buschbeck et al. (2012) investigated how the in-cylinder flow field affected combustion dynamics, they found the

variations in the kinetic energy of the flow field are primarily responsible for the CCV of the combustion process at stoichiometric engine operation, whereas, at lean operation, the velocity distribution in the flow field causes a macroscopic motion of the flame kernel, which has a significant impact on the combustion process. Recently, Welch et al. (2022) conducted high-speed PIV and flame imaging experiments under various levels of homogeneously mixed external EGR to investigate the causal chain for fired CCV in a port fuel injection (PFI) SI engine. The results showed that large-scale velocity motion significantly influences the flames, the slower flames occurring at higher EGR levels present greater sensitivity to the variations of the velocity field. And in the most extreme cycles with the greatest EGR level, whether the flame propagates towards the cylinder's center or whether it sustains growth by propagating within the lingering tumble vortex depends on the status of the large-scale velocity structures at the ignition timing. Therefore, it is crucial to gain a thorough grasp of the in-cylinder flow characteristics for effectively monitoring and controlling the combustion CCV of SI engines.

To reduce the CCV of the in-cylinder flow field, previous research examined the effect of various engine geometries on different flow fields. And some effective techniques were developed and employed to change the strength of the large-scale flow structure (tumble or swirl) within the cylinder and the duration of high turbulence intensity near the spark plug position in the late compression stage. The basic elements related to the control of the in-cylinder flow field are the cylinder head geometry variation including the change of intake valve diameter and modification to the exit of the intake port (Freudenhammer et al. 2015), the piston top contour variation (Yin et al. 2016), the adoption of variable intake valve timing or lift (Liu et al. 2012; Bücker et al. 2013), the modifications to intake valve profiles and intake ports to produce different tumble ratio (Omura et al. 2016), the insertion amplitude of a control flap near the intake valve to modify the in-cylinder flow fields (Vu and Guibert 2012), closing or opening of the tumble control flap mounted on the intake port to generate different intensities tumble flow (Zhang et al. 2015; Li et al. 2017), and swirl flow introduced into tumble flow by a swirl control valve installed in one of the intake ports (Towers and Towers 2004; Wang et al.2016). Among these methods for CCV control of the in-cylinder flow field, using a charge motion control valve in the intake system has been proven to be a flexible and effective option, especially the tumble control flap, which is widely used in SI engines.

To further understand the CCV features of the in-cylinder flow field, various analysis techniques built on the post-processing of velocity field data obtained from experiments or simulations have been developed. Fast Fourier Transform (FFT) (Funk et al. 2002; Li et al. 2004, 2017; Joo et al. 2004; Liu et al. 2012) and proper orthogonal decomposition (POD) (Roudnitzky et al. 2006; Wang et al. 2015; Zhang et al. 2015; Gao et al. 2019; Rulli et al. 2021; Wu et al. 2022) are widely used filtering techniques to decompose the in-cylinder instantaneous velocity field into three parts: the mean part, the low-frequency coherent part, and the high-frequency incoherent turbulent part. The coherent part considered to be associated with the flow CCV is then extracted and used to evaluate the CCV of the in-cylinder turbulent flow. Wang et al. (2016) employ the relevance index to evaluate the CCV of the in-cylinder flow field at different crank angles during the engine cycle in a specific swirl plane with two different swirl flow conditions. The basic idea of this technique is to compare the similarity of the flow fields at the same crank angle in different cycles. As mentioned earlier, the CCV of the flow field close to the spark plug at the ignition timing significantly affects the developing flame kernel and the subsequent rate of combustion. However, these analysis techniques are commonly used to clarify the development of the CCV of the in-cylinder flow, or to elucidate the relationship between the in-cylinder tumble

or swirl motion and the flow CCV, and do not establish much connection with subsequent combustion CCV. In a recent study, Matsuda et al. (2021) used a correlation map analysis technique to investigate the factors influencing the flow CCV at the plug position at the ignition timing in a high-tumble four-stroke optically accessible engine with Miller cycle by time-resolved PIV measurements. The correlation was traced back to the flow distribution in the intake and compression strokes. The results showed that the flow direction at the plug position at the ignition timing is affected by three factors: the position of the stagnation plane between the intake jet from the intake valves' bottom side and the upper side of the tumble vortex, the blowback flow into the intake port caused by the Miller cycle during the early compression stroke, and the position of the tumble vortex during the late compression stroke. This technique was also used to analyze the interaction between flow and spray or combustion (Stiehl et al. 2016; Laichter and Kaiser 2022).

To sum up, the flow characteristics and the factors influencing the flow CCV at the plug position at the ignition timing are still not well understood in realistic engine geometries equipped with a charge motion control valve. Consequently, the topic of this paper has shifted from the CCV of the bulk flow to the CCV of the flow at the spark plug position at the ignition timing. The experiments are conducted in an optically accessible single-cylinder, spark-ignition engine equipped with a tumble control flap by using a high-speed PIV measurement. To build the relationship between the flow at the spark plug position and the flow distribution during the intake and compression stroke in time and space, a correlation map analysis is employed. The proper orthogonal decomposition (POD) method is used to extract the large-scale coherent structures and then reconstruct the flow fields to improve the correlation between the above two. These experimental results will build a bridge to connect the CCV of the in-cylinder flow and the CCV of the combustion. The paper is organized as follows. In Sect. 2, the optical engine and experimental setup are described. The flow field analysis methodologies including POD used for extracting large-scale flow CCV components and the correlation maps analysis used for building the relationship between flow at the plug position at the ignition timing and the flow distribution in the intake and compression strokes are presented in Sect. 3. Section 4 presents the results and discussion. The main conclusions are summarized in the last section.
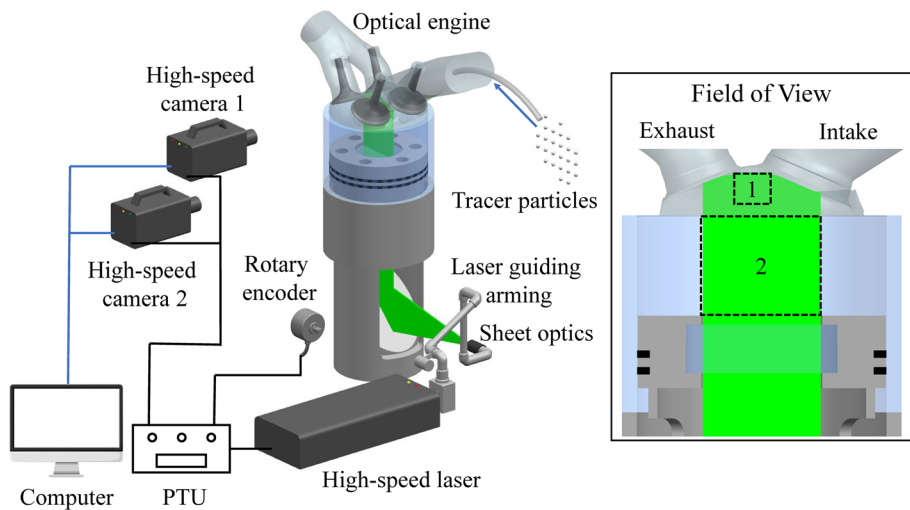
2 Experimental Setup

2.1 Optical SI Engine

The experimental measurements were carried out in an optically accessible single-cylinder, four-stroke, four-valve, SI engine. A production-type cylinder head with a pent-roof combustion chamber and a charge motion control valve was used in this experiment. Table 1 lists the detailed specifications of the SI optical engine, and Fig. 1 presents the schematic of the PIV measurement system and the experimental configuration of the optical engine. A transparent quartz piston window provides optical access for the vertically propagating laser sheet, which illuminates the center plane of the tumble flow in the region between the intake and exhaust valves. A spark plug dummy flush with the cylinder head surface was utilized in place of the original spark plug. To capture the flow field in the combustion chamber, a small viewing hole with a flat quartz window was machined in the production-type cylinder head with minimal alteration to the original geometry. Consequently, the

Table 1 Specifications of the SI optical engine

Component	Scales
Bore [mm]	82.5
Stroke [mm]	90
Connecting rod [mm]	168
Cycle	4 strokes
Intake/exhaust valves	2/2
Compression ratio	9.6:1
Intake valve open (IVO) [CAD]	−13
Intake valve close (IVC) [CAD]	242
Exhaust valve open (EVO) [CAD]	470
Exhaust valve close (EVC) [CAD]	9
Engine speed [rpm]	800
Intake top dead center [CAD]	0

Fig. 1 Schematic of the PIV measurement system and the experimental configuration of the optical engine

transparent quartz cylinder liner and the flat quartz window in the cylinder head constitute two optical windows for two high-speed cameras.

Two different in-cylinder tumble intensities were investigated by controlling the tumble flap inserted in the intake manifold. The low tumble ratio (LTR) case relates to the flap being fully open, whilst the high tumble ratio (HTR) case refers to the flap being entirely closed. Figure 2 presents the schematic of the relationship between the tumble level and the flap position.

2.2 PIV Setup

A high repetition rate commercial PIV system (LaVision) was used to measure the flow field in the experiment. Di-ethylhexyl-sebacat (DEHS) droplets as the PIV tracer particles

Fig. 2 Schematic of the relationship between the tumble intensity and the flap position
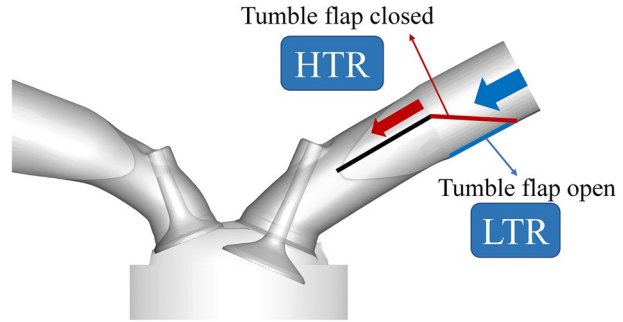
with an average diameter of approximately 1 μm were produced by a Laskin sprayer and then fed into the in-cylinder with the intake air via the inlet of the intake manifold. The light source used for illuminating the first and second images of tracer particles was a dual pulse single head Nd: YLF laser (LDY-303HE, wavelength: 527 nm, allowed frequency range 0.2–20 kHz, maximum output energy at 2.4 kHz: about 12.5 mJ/pulse). The two laser beams were combined by using polarisers and exited through a single port of the laser head, then converted to laser sheets by integrated light sheet optics mounted with the laser guiding arm. A 45° mirror inside the piston reflected the two overlapping laser sheets upward to illuminate the tumble plane through the transparent quartz piston window, and the thickness of the laser sheets was adjusted to less than 1 mm in the measurement region. Mie scattering signals from the tracer particles were filmed with two high-speed 12-bit CMOS cameras (High-speed Star, full-chip with 1024 pixels × 1024 pixels at 2.4 kHz) mounted with a 200 mm f/5.6 Nikkor lens, and the projected pixel size of the camera in the imaging plane is 20 μm. Camera 1 was used to capture the local flow field covering the location of the original spark plug in the combustion chamber, while camera 2 recorded the global flow field in the cylinder, as shown in Fig. 1.

2.3 Data Acquisition and Processing

The data acquisition and processing were performed on the commercial software DaVis 8.3.0. In data acquisition, the trigger timing of the double laser pulses and operation of the electronic shutter on the CMOS cameras were synchronized with a Programmable Timing Unit (PTU, LaVision). The system trigger signal was a crank angle signal from a rotary encoder mounted directly to the crankshaft. Images were captured every 2° CA during intake and compression strokes from 60 to 330 CAD at 2.4 kHz with a constant motored speed of 800 rpm. The time interval (dt) between the two laser pulses for the LTR and HTR conditions were set to 20 μs and 12 μs, respectively. In data processing, the standard cross-correlation PIV algorithm for vector field calculation is the same for the field of view 1 (FOV 1) and 2 (FOV 2) image pairs, which with a decreasing interrogation window size scheme. In the field of view 1, the first two passes used a 128 pixels × 128 pixels square interrogation window and were followed by three passes using a 64 pixels × 64 pixels round interrogation window, in the field of view 2 the decreasing interrogation window sizes were set to 64 pixels × 64 pixels and 32 pixels × 32 pixels respectively. For both the field of view, the first passes used 75% overlap and the second one was set as 50%. As a result, the maximum displacements of particles were 2–13 pixels in the field of view 1 under both conditions. In the field of view 2, the maximum displacements were less than

8 pixels except for a maximum displacement of 12 pixels for 60 CAD under LTR conditions. On the whole, the settings of *dt* under LTR and HTR conditions were reasonable for meeting the maximum displacement value of 1/4 (or less) of the interrogation window size criterion suggested by Keane and Adrian (1990). The final obtained flow field sizes were 12 mm × 10 mm and 52 mm × 64 mm, and the vector spacing of 0.48 mm × 0.48 mm and 1.21 mm × 1.21 mm were achieved in the field of view 1 and 2, respectively.

The PIV measurement parameters mentioned above for the field of views 1 and 2 are listed in Table 2.

3 Flow Field Analysis Methodology

3.1 Method for Extracting CCV Components

Since the in-cylinder flow within IC engines is turbulent, the ensemble-averaged (also known as phase-averaged) technique is widely employed to decompose the instantaneous velocity u into an ensemble-averaged component $\bar{u}$ (multi-cycle mean at the given crank angle) and fluctuation component u':

$$u = \bar{u} + u' \tag{1}$$

However, this method cannot effectively obtain the real turbulent component of the in-cylinder flow due to the fluctuation component containing both the flow CCV component u'_{CCV} and the turbulent component u'_{turb}. In other words, the fluctuation component cannot be directly recognized as the turbulent component as like in steady-state flow, particularly in gasoline engines. According to previous research on the in-cylinder flow, small-scale

Table 2 PIV measurement parameters for the field of views 1 and 2

Items	Details in field of view 1	Details in field of view 2
Size of the flow field	12 mm × 10 mm (width × height)	52 mm × 64 mm (width × height)
Camera sensor resolution	1024 pixels × 1024 pixels	
Sampling frequency	2.4 kHz	
Image pair number	108	
Frame interval	20 μs at LTR / 12 μs at HTR	
Tracing particles	DEHS	
Light source	Nd: YLF laser, maximum output energy at 2.4 kHz: about 22.5 mJ/ pulse	
Light wavelength	527 nm	
Light thickness	Less than 1 mm	
Interrogation window size	128 pixels × 128 pixels to 64 pixels × 64 pixels	64 pixels × 64 pixels to 32 pixels × 32 pixels
Filter method	Smoothing	
Interrogation window overlap	75% to 50%	
Spatial resolution	0.48 mm × 0.48 mm	1.21 mm × 1.21 mm

structures are believed to be isotropic and large-scale structures are associated with the CCV of the flow (Müller et al. 2010). Therefore, it is necessary to separate the flow CCV and turbulent components with a suitable method.

Many researchers have developed decomposition methods for the flow CCV and turbulence components from the experimental data, such as the proper orthogonal decomposition (POD) method (Roudnitzky et al. 2006; Wang et al. 2015; Zhang et al. 2015; Gao et al. 2019; Rulli et al. 2021; Wu et al. 2022) spatial Gaussian filter (Reuss 2000; Funk et al. 2002), and temporal frequency analysis (Jarvis et al. 2006; Okura et al. 2014). In this study, the POD method is utilized, and a brief description of the POD algorithm is given below.

POD is based on the concept of decomposing an original velocity field into a sequence of linear space-dependent functions (POD modes) and their corresponding time-dependent coefficients. Two distinct POD approaches exist: the classical POD introduced by Lumley (1967) and the snapshot POD proposed by Sirovich (1989). In this work, since the number of gathered cycle samples is far less than the number of spatially discretized points, snapshot POD was applied to improve computational accuracy and efficiency. The velocity temporal correlation tensor in snapshot POD is defined as the inner product of two snapshots, specific to the in-cylinder flow, that is, two velocity fields at the same spatially discretized point at the given crank angle but two different cycle samples, expressed as follows:

$$R\left(u^{(i)}, u^{(j)}\right) = \sum_{n=1}^{N_x} \left[\sum_{d=1}^{D} \left(u_d^{(i)}(x_n) u_d^{(j)}(x_n) \right) \right] = N \cdot C_{ij} \tag{2}$$

where i and j denote two different cycle samples at the given crank angle; N_x is the total number of spatially discretized points; D is the number of space dimensions, $d=1$ and $d=2$ correspond respectively to the horizontal and vertical velocity components; N is the total number of cycle samples; C_{ij} is the spatial correlation matrix with a size of $N \times N$. The eigenvalues and the corresponding eigenvector are obtained by computing the following equation:

$$\begin{bmatrix} C_{11} & \cdots & C_{1N} \\ \vdots & \ddots & \vdots \\ C_{N1} & \cdots & C_{NN} \end{bmatrix} \begin{bmatrix} A_1 \\ \vdots \\ A_N \end{bmatrix}^{(k)} = \lambda^{(k)} \begin{bmatrix} A_1 \\ \vdots \\ A_N \end{bmatrix}^{(k)} \tag{3}$$

Each POD mode denoted as $\psi_d^{(k)}$ can then be calculated from the linear combination of the products between the eigenvector components and the original flow field as shown below:

$$\psi_d^{(k)}(x_n) = \sum_{m=1}^{N} \left[A_m^{(k)} u_d^{(m)}(x_n) \right] \tag{4}$$

Similarly, each time-dependent coefficient denoted as $a^{(k)}(\theta_{CA})$ (here the time corresponding to crank angle θ_{CA}) can be deduced from the projection of the original velocity fields onto the corresponding kth POD mode:

$$a^{(k)}(\theta_{CA}) = \left(u^{(i)}, \psi^{(k)}\right) = \sum_{n=1}^{N} \left[\sum_{d=1}^{D} \left(u_d^{(i)}(x_n) \psi_d^{(k)}(x_n) \right) \right] \tag{5}$$

Finally, the original instantaneous velocity field at a given crank angle θ_{CA} can be reconstructed with the following equation:

$$u(x, \theta_{CA}) = \sum_{k=1}^{N_{mode}} \left[a^{(k)}(\theta_{CA}) \psi^{(k)}(x) \right] \tag{6}$$

where N_{mode} is the total mode number equal to N.

The POD code used in this paper is the same as in our previous papers (Wang et al. 2015; Zhang et al. 2015), and a phase-dependent POD quadruple decomposition was employed to address the ambiguity in defining the cutoff mode number. The fundamental concept is to divide the instantaneous flow field into four parts, described as follows:

$$u(x, \theta_{CA}) = u_{mean}(x, \theta_{CA}) + u_{coherent}(x, \theta_{CA}) + u_{transition}(x, \theta_{CA}) + u_{turbulent}(x, \theta_{CA}) \tag{7}$$

where the term $u(x, \theta_{CA})$ is the instantaneous flow field at a given crank angle θ_{CA}; the first term u_{mean} (corresponding to this single cycle, not multi-cycle mean at the given crank angle) on the right side is the mean part characterizing the entire motion morphology of the flow field and accounting for the majority of the kinetic energy; the second term $u_{coherent}$ refers to the coherent part encompassing the large-scale coherent structure and covering most of the fluctuation energy of the flow field; the third term $u_{transition}$ defined as the transitional part that plays a role on achieving the energy transportation from the large-scale vortices to smaller ones; the last term $u_{turbulent}$ corresponds to the turbulent part representing the small-scale vortex structures and containing only a modest amount of kinetic energy of the flow field. A detailed description of the determination of the cutoff mode for each decomposition part is given by Wang et al. (2015) and Zhang et al. (2015).

Numerous investigations on in-cylinder flow CCV have demonstrated that the unstable coherent structures of the flow field were mostly responsible for initiating the cyclic variations (Qin et al. 2014; Wang et al. 2015; Liu et al. 2022). Therefore, the reconstructed velocity field containing only the mean and coherent parts was used for subsequent data analysis, and defined as the bulk flow u_{bulk} as follows:

$$u_{bulk} = u_{mean} + u_{coherent} \tag{8}$$

While the reconstructed velocity field containing the transitional and turbulent two parts was defined as the turbulence component u'_{turb}:

$$u'_{turb} = u_{transition} + u_{turbulent} \tag{9}$$

3.2 Correlation Maps Analysis

The goal of this research is to identify the dominant factors that influence the flow CCV at the spark plug position at the ignition timing under various in-cylinder tumble intensities. Similar to the works of Bode et al. (2017) and Matsuda et al. (2021), a statistical analysis evaluated by a correlation coefficient is applied to identify correlations between the flow field at the spark plug position at the ignition timing $u_{spark\text{-}plug}$ and the flow field on the measurement plane u_{bulk} in space and time. The correlation coefficient is defined as follows:

$$R = \frac{\sum_{i=1}^{N} \left(A_i - \overline{A} \right) \left(B_i - \overline{B} \right)}{\left\{ \left[\sum_{i=1}^{N} \left(A_i - \overline{A} \right)^2 \right] \cdot \left[\sum_{i=1}^{N} \left(B_i - \overline{B} \right)^2 \right] \right\}^{1/2}} \tag{10}$$

where $\overline{A}$ and $\overline{B}$ are the ensemble average of databases A and B, respectively; N is the total number of cycle samples. In this work, the flow direction $\theta_{spark\text{-}plug}$ calculated based on a vector at the spark plug position at the ignition timing was chosen for database A as the characteristic parameter of $u_{spark\text{-}plug}$. The component of bulk flow u_{bulk} projected onto the ensemble-averaged flow $\overline{u}$, denoted as $U_{EAF}(x, \theta_{CA})$, was selected for database B as the characteristic parameter of u_{bulk} at position x at crank angle θ_{CA}. It is defined as follows:

$$U_{EAF}(x, \theta_{CA}) = \frac{u_{bulk}(x, \theta_{CA}) \cdot \overline{u}(x, \theta_{CA})}{\left|\overline{u}(x, \theta_{CA})\right|} \tag{11}$$

A better understanding of the correlation coefficient method conducted in this study may be gained from Fig. 3. The flow direction $\theta_{spark\text{-}plug}$ was correlated with each $U_{EAF}(x, \theta_{CA})$ within the measurement plane at different crank angles.

The variation range of correlation coefficients is $[-1, 1]$: ± 1 denotes an absolutely linear correlation between databases A and B, whereas 0 refers to total uncorrelation, $|R| < 0.3$ implies a low degree, $0.3 < |R| < 0.5$ some degree, $0.5 < |R| < 0.7$ a significant degree, and $|R| > 0.7$ a high degree of dependence (Holický 2013, pp. 142–144). For results between -1 and 1, a two-sided statistical t-test was employed to evaluate the confidence level. The H_0-hypothesis was defined as the statistical independence of databases A and B ($R = 0$), and its rejection means that the two investigated objects A and B are assumed to be correlated to a certain degree. In this paper, the cycle sample number n is 108, the error probability α was set to 1%, and the test quantity $t_{(\alpha,n)} = t_{(0.01, 108)} = 2.62$ can be deduced from the tabulated thresholds (Montgomery and Runger 2010). For a known cycle sample number n, the H_0-hypothesis was checked by computing the test quantity as follows:

$$t_{AB} = R\sqrt{\frac{n-2}{1-R^2}} \tag{12}$$

Fig. 3 Demonstration of correlation coefficient method used in this study. Database A corresponds to the flow direction at the spark plug position at the ignition timing; database B corresponds to the velocity vector fields U_{EAF} within the measurement plane at different crank angles. The red dot indicates the spark plug position
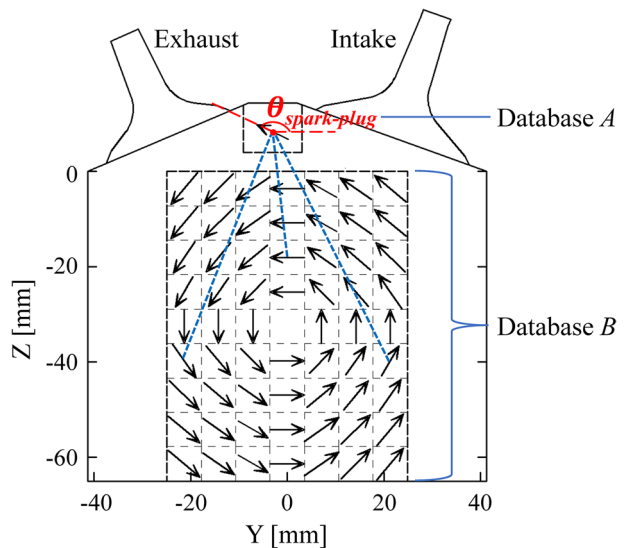
For H_0-hypothesis to be rejected, $t_{AB} > t_{(0.01, 108)}$ needs to be satisfied. Finally, it is calculated that $|R| > 0.247$ is the confidence interval.

4 Results and Discussion

4.1 Flow Field Reconstruction Based on Phase-Dependent POD

An illustration of the reconstructed velocity fields based on the phase-dependent POD method at 240 CAD of the LTR condition is demonstrated in Fig. 4. It can be observed that the large-scale flow structure is contained in the bulk flow u_{bulk}, whereas the small-scale
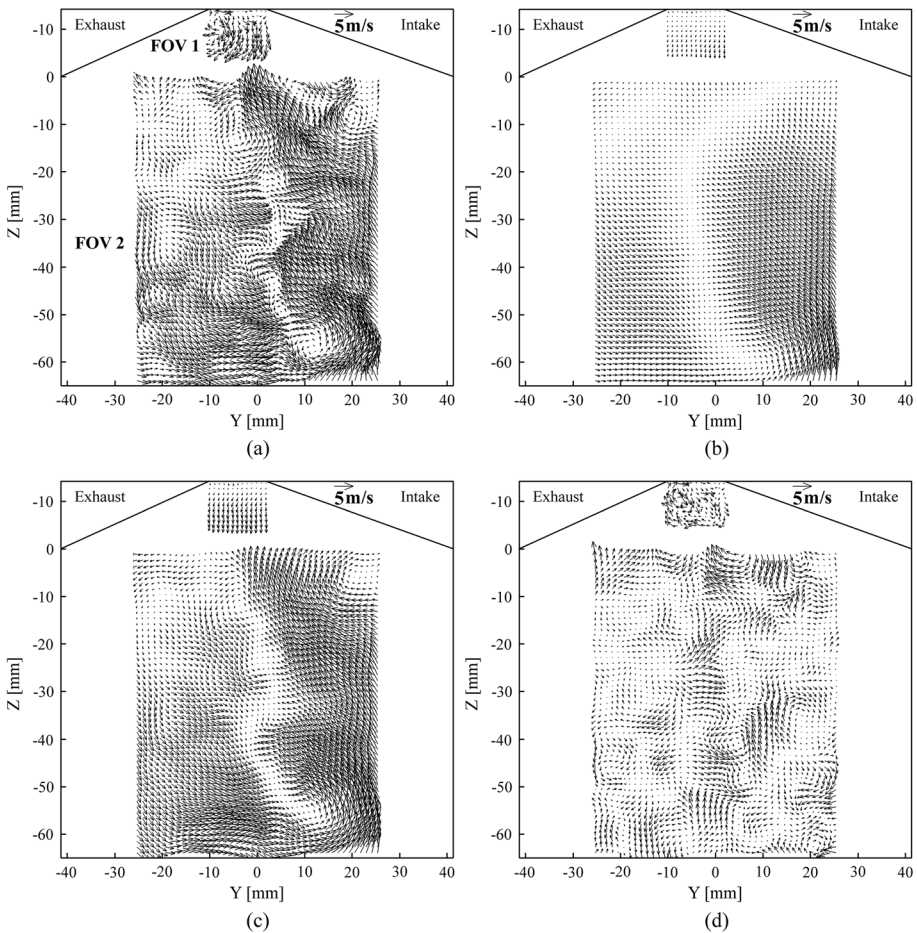
Fig. 4 Demonstration of the flow field decomposition at 240 CAD of the LTR condition: **a** the original transient velocity field u, **b** the ensemble-averaged velocity field $\bar{u}$, **c** the bulk flow u_{bulk}, and **d** the turbulence component u'_{turb}. Every second vector is shown in the FOV 1

flow structure is retained by the turbulence component u'_{turb}. Furthermore, the local vortex structure and tumble vortex position in the bulk flow u_{bulk} differ from the ensemble-averaged flow $\bar{u}$ because the bulk flow u_{bulk} comprises the CCV component, primarily the large-scale coherent structure. These results indicate that POD is an effective method for flow CCV component extraction in this study.

4.2 Velocity Field Distribution at the Spark Plug at the Ignition Timing

The focus of this paper is to explore the factors that affect the flow cycle variation at the spark plug position at the ignition time under two different tumble flow intensities. The ignition time corresponds to 330 CAD in this study. Figure 5 presents the ensemble-averaged velocity field distributions at 330 CAD for the LTR and HTR conditions. From the perspective of global flow, there is no discernible tumble flow trend in the cylinder under the LTR condition, the flow is mainly influenced by the upward movement of the piston. In contrast, under the HTR condition, the tumble flow trend in the cylinder is quite identifiable, and strong flow shear is applied to the top surface of the piston and the bottom surface of the combustion chamber.

Returning to the flow at the spark plug position, the overall flow trend of the flow field is comparable between the two operating conditions, with the flow nearly parallel to the bottom surface of the combustion chamber from the intake valve side toward the exhaust
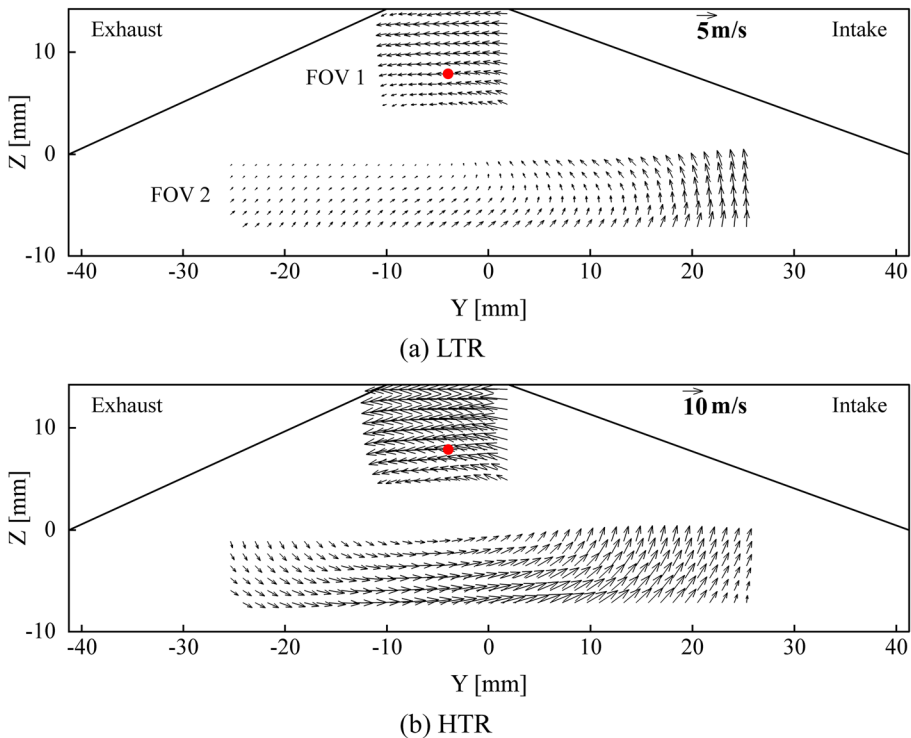

Fig. 5 Distribution of ensemble-averaged velocity fields under **a** LTR and **b** HTR conditions at 330 CAD. The red dot refers to the spark plug position, and every second vector is shown in the field of view 1

valve side. However, velocity is much greater than that in the LTR condition. To further
determine the degree of flow cyclic variation at the spark plug position under two work-
ing conditions, the magnitude and direction angle of velocity at the spark plug position
between different cycles at the time 330 CAD were extracted and evaluated.

Figure 6 depicts the frequency distribution of magnitude and direction angle of veloc-
ity at the spark plug position under two working conditions. The instantaneous bulk flow
velocity of each cycle is normalized by local ensemble-averaged velocity. Beginning at
zero on the intake side of the horizontal axis, the direction angle increases counterclock-
wise. The velocity magnitude and the direction angle fall within a wide distribution range
under the LTR condition. The velocity with the highest frequency is close to the ensemble-
averaged velocity Ve, and the values of velocity ranging from 0.25 to 1.75 accounts for a
considerable amount. In addition, the distribution of direction angle varies between 145°
and 215°, which spans a range of 70°. However, the velocity magnitude and direction angle
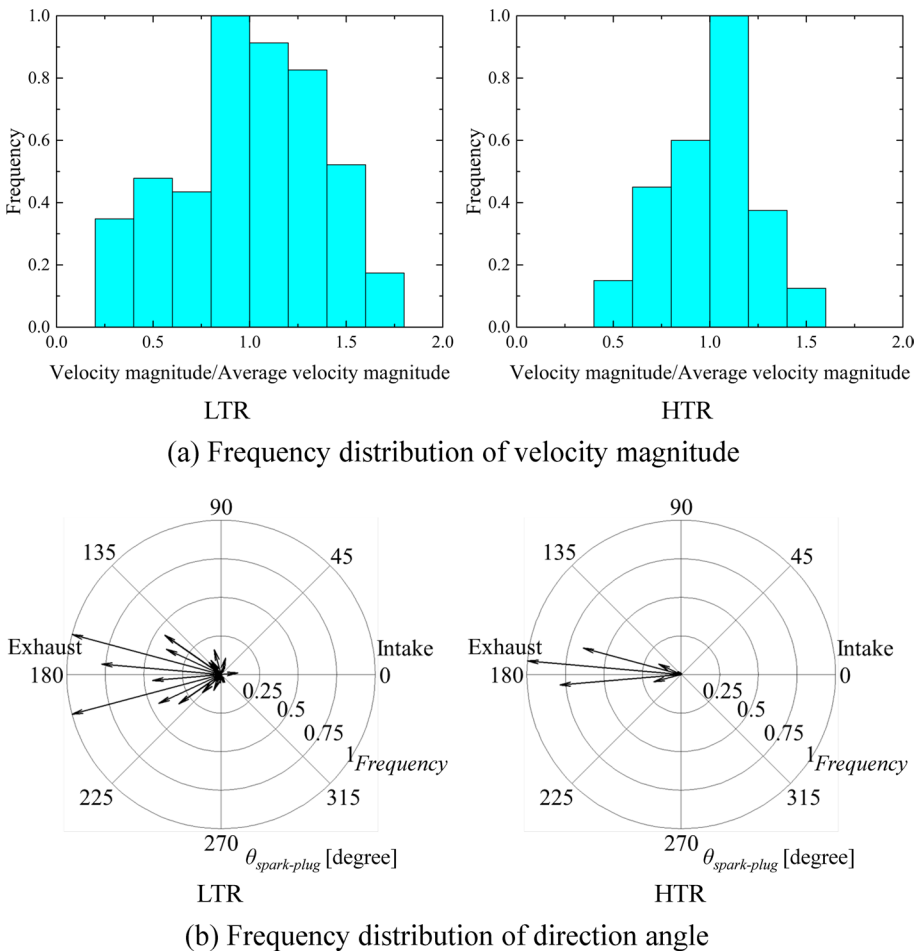exhibits a concentrated distribution trend for the HTR conditions. The velocity magnitude

(a) Frequency distribution of velocity magnitude

(b) Frequency distribution of direction angle

Fig. 6 Frequency distribution of the velocity magnitude and direction angle under LTR and HTR conditions
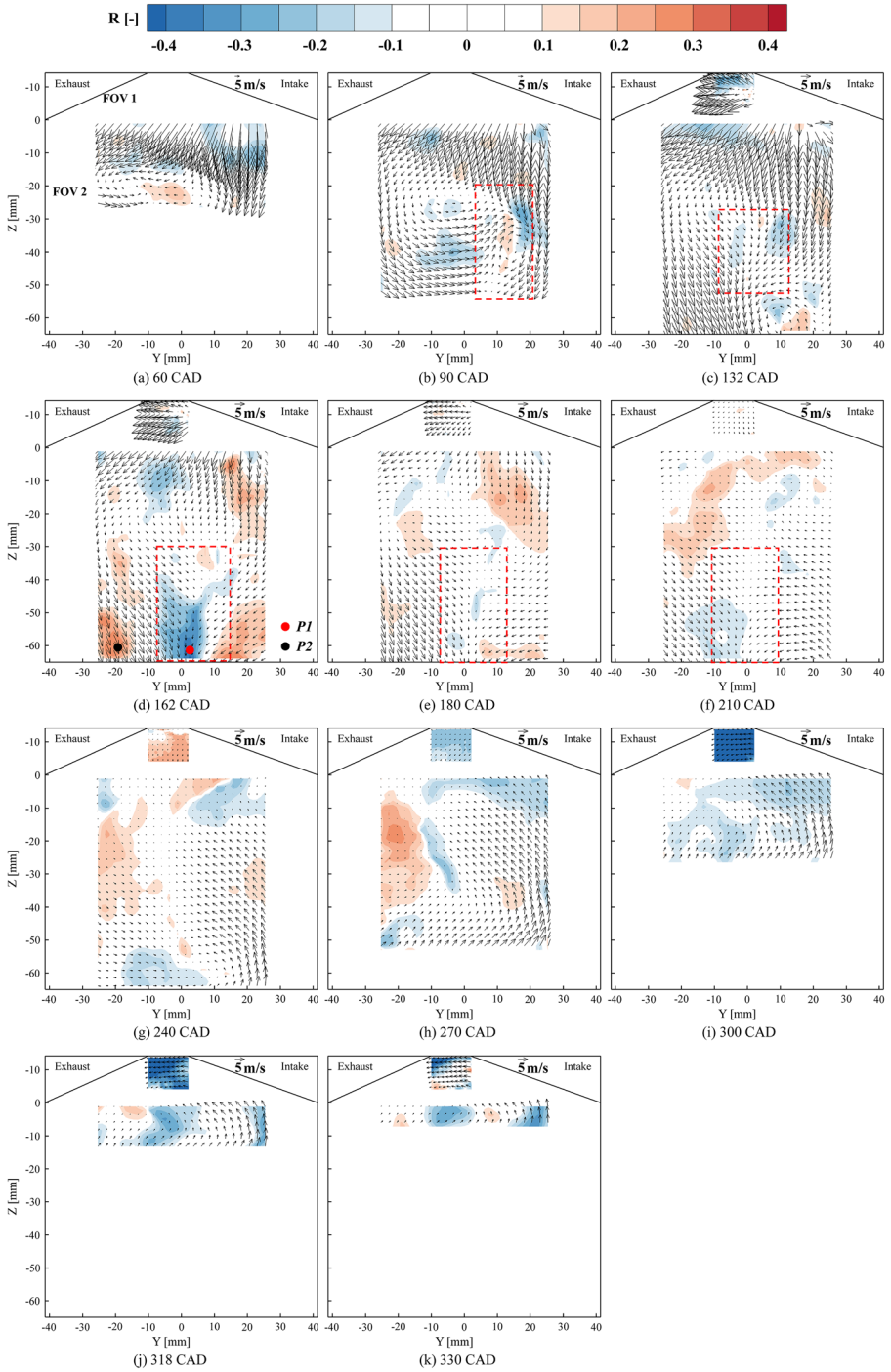at the spark plug position at 330 CAD

Fig. 7 Correlation R of the direction angle $\theta_{spark\text{-}plug}$ at the spark plug position at the ignition time with the ▶
component of the bulk flow projected onto the ensemble-averaged flow U_{EAF} at selected CAD. The corresponding operating condition is LTR. The flow fields of 60 CAD and 90 CAD in the FOV 1 region are missing due to the block out of the intake valve. Every third vector is shown in FOV 1, and every second vector is shown in FOV 2. The vectors represent the mean flow

is concentrated close to the ensemble-averaged velocity, while the direction angle is primarily distributed between 165° and 185°, with only a 20° range. The above comparison reveals that the flow cycle variation at the spark plug position at the ignition time is dramatically reduced under the HTR condition. To identify the dominant factors influencing the flow cycle variation at the spark plug position at the ignition time under two operating conditions, the velocity direction angle was chosen as the representative value of the flow in the following correlation map analysis.

4.3 Factors Influencing the CCV of the Flow Direction at the Spark Plug Position at the Ignition Timing Under the LTR Condition

The correlation coefficient, as defined in Eq. (10), is employed to find the factors influencing the CCV of the flow direction at the spark plug position at the ignition timing. The databases *A* and *B* correspond to the direction angle of flow at the plug position at the ignition timing $\theta_{spark\text{-}plug}$ and the component of the bulk flow projecting onto the ensemble-averaged flow U_{EAF} within the measurement plane at different crank angles, respectively.

Figure 7 demonstrates the correlation map results under the LTR condition. Since the tumble flap is open under the LTR condition, the fresh air splits into two annular jets that enter the cylinder from the upper and lower sides of the intake valve, respectively. Constrained by the cylinder wall and the top surface of the piston, the flow of two annular jets will be redirected and converged into the cylinder (as shown by the evolution of the flow field on the tumble center plane at the 60 CAD and 90 CAD), after which the two jets will collide and merge into a tumble flow within the cylinder. Before 132 CAD, the intake jet flow on the exhaust side plays a vital role in the flow structure within the cylinder, and the collision region (marked in a red box) of the two jet flows is predominantly skewed toward the intake valve side. However, the regions of high correlation are small and inchoate, which makes them impossible to be clearly observed. To better show the comparison of the correlation map at various crank angles, the confidence interval of correlation coefficients in the maps decreases to $|R| > 0.1$ under the LTR condition, that is, the color map of R between − 0.1 and 0.1 is set to white color. After 132 CAD, the collision region moves towards the lower middle of the cylinder when the intake valves are gradually closing with the piston moving downward. At approximately 162 CAD, a zone of high negative correlation develops around the collision region of two jet flows, while the regions where two jet flows are located present a high positive correlation. However, the zones of significant negative and positive correlation nearly disappear at 180 CAD and 210 CAD, even though the collision between the two jet flows is still occurring. Around 240 CAD, a weak large-scale tumble flow emerges and is subsequently forced upward by piston movement. Although correlation exists in some locations, such as near the tumble vortex and the flow separation region, the correlation coefficients are less than at 162 CAD. After 240 CAD, as the piston continues to move upwards, the influence of tumble motion on the flow field close to the spark plug grows. The main characteristic of the change during 270 CAD and 330 CAD in the FOV 1 region is that the average velocity magnitude gradually increases and the flow direction tends to be uniform (confirmed by the discussion results in Sect. 4.5

(a) 60 CAD

(b) 90 CAD

(c) 132 CAD

(d) 162 CAD

(e) 180 CAD

(f) 210 CAD

(g) 240 CAD

(h) 270 CAD

(i) 300 CAD

(j) 318 CAD

(k) 330 CAD

below). Compared with the bulk flow in the FOV2 region, the negative correlation R in the FOV1 region increases gradually and reaches a high at around 300 CAD due to the gradual enhancement of flow shear with the combustion chamber wall. After that, the negative correlation R of the FOV1 region gradually weaken, as shown in Fig. 7 at 318 CAD and 330 CAD. The above correlation map results indicate that the collision position of the intake jets at the end of the intake stroke and flow shear with the combustion chamber wall at the late compression stroke have the most significant influence on the direction angle of flow at the ignition time of the spark plug position.

To further deepen the understanding of the correlation coefficient used in this study, the U_{EAF} at positions of $P1$ and $P2$, which correspond to the local minimum and maximum value of the correlation coefficient at 162 CAD, were extracted and plotted versus the direction angle at the spark plug position at the ignition timing, as shown in Fig. 8. The U_{EAF} values at these two points were both positive in all cycles. A positive U_{EAF} value indicates that the flow at that point was in the same direction as the ensemble-averaged flow. The distributions of the scatter plot at points $P1$ and $P2$ appear to drop and rise monotonically, respectively. When the U_{EAF} is low in the negative correlation coefficient and high in the positive correlation coefficient, the direction angle tends to have a high value.

As analyzed above, the collision position of the intake jets at the end of the intake stroke under the LTR condition seems to be a dominant factor in causing the CCV of the direction angle of flow at the spark plug position at the ignition time. To further understand the CCV of the flow field distribution associated with the collision position of the intake jet at 162 CAD and how that collision position affects the flow field distribution at subsequent crank angles, the correlation coefficient method continues to be used to build the relationship beginning at an earlier crank angle. In this section, the component of the bulk flow projected onto the ensemble-averaged flow at point $P1$ at 162 CAD is defined as U_{P1}, and databases A and B correspond to the U_{P1} and the component of the bulk flow projected onto the ensemble-averaged flow U_{EAF} within the measurement plane at different crank angles, respectively. Figure 9 demonstrates the correlation map.

During the early and middle stages of the intake stroke, the correlation coefficient could be observed at the regions where two intake jets pass through (marked in a blue box), as
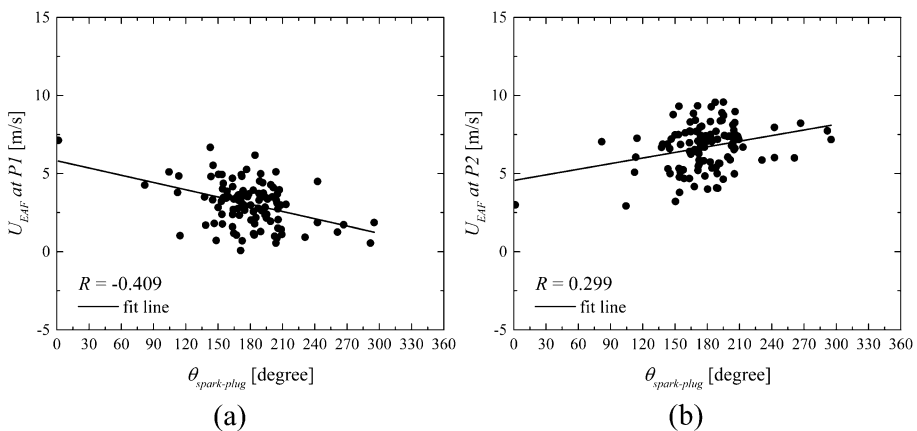

Fig. 8 Scatter plot between the component of the bulk flow projected onto the ensemble-averaged flow U_{EAF} at $P1$ and $P2$ in the collision region at 162 CAD and the direction angle $\theta_{spark-plug}$ at the spark plug position at the ignition timing
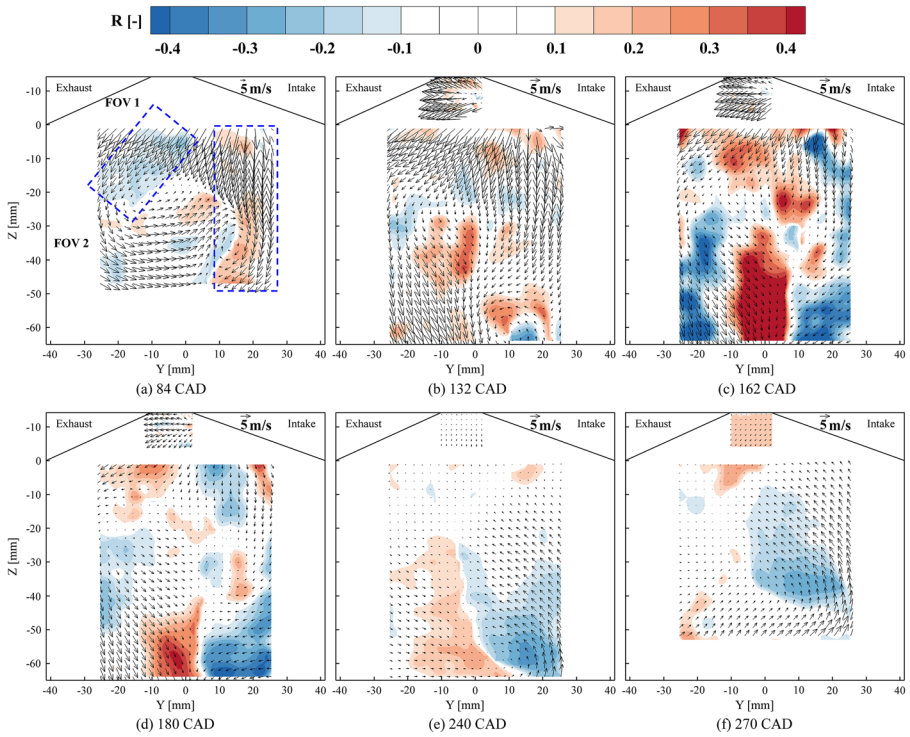
Fig. 9 Correlation map analysis for the component of the bulk flow projected onto the ensemble-averaged flow U_{P1} at point $P1$ at 162 CAD and the component of the bulk flow projected onto the ensemble-averaged flow U_{EAF} at selected CAD. The flow field of 84 CAD in the FOV 1 region is missing due to the block out of the intake valve. Every third vector is shown in FOV 1, and every second vector is shown in FOV 2. The vectors represent the mean flow

shown at 84 CAD. In addition, adjacent positive and negative correlation areas around a local vortex are generated from the collision of the two intake jets, as shown at both 84 CAD and 132 CAD. These results indicate that the collision position of the intake jets at 162 CAD is mainly connected to the strength of the two intake jets and the position of the local vortex in the early and middle stages of the intake stroke. After 162 CAD, the high correlation coefficients appear in the regions influenced by the collision of the intake jets and the subsequent weak tumble flow formed by the merger of the intake jets.

4.4 Factors Influencing the CCV of the Flow Direction at the Plug Position at the Ignition Timing Under the HTR Condition

Figure 10 presents the correlation map under the HTR condition. As illustrated in Fig. 3, the majority of the fresh air as a single annular jet enters the cylinder from the upper side of the intake valve under the HTR condition when the intake flap is closed. Then the tumble flow motion with an apparent counterclockwise large-scale vortex structure forms in the early stage of the intake stroke. Furthermore, the tumble flow maintains intensity until the late compression stroke.
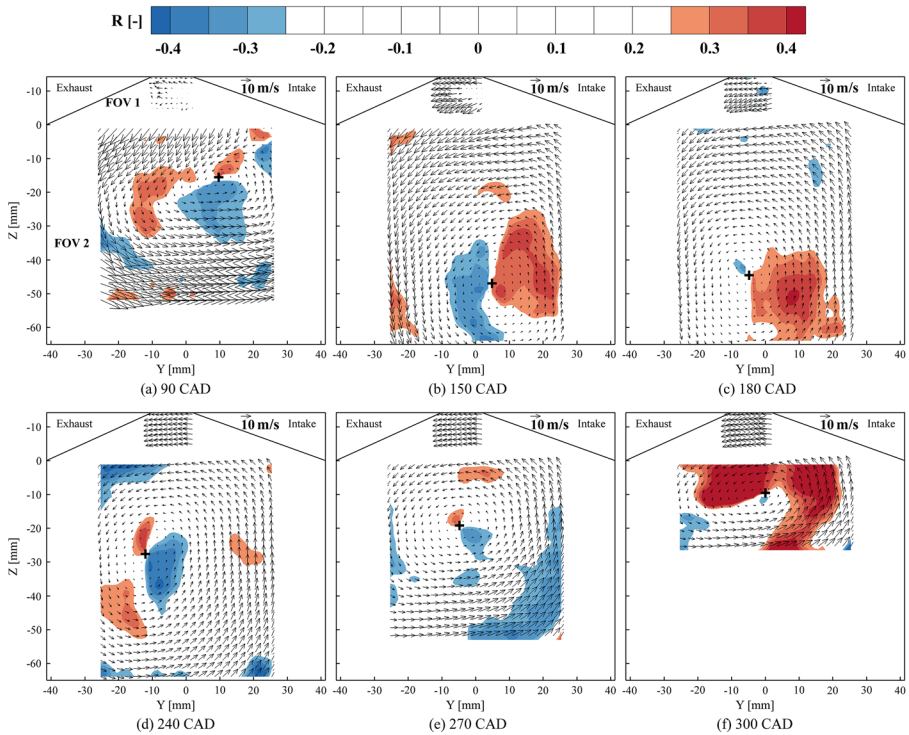
Fig. 10 Correlation map analysis for the direction angle at the spark plug position at the ignition time and the component of bulk flow projected onto the ensemble-averaged flow U_{EAF} at selected CAD. The corresponding operating condition is HTR. Every third vector is shown in FOV 1, and every second vector is shown in FOV 2. The black cross refers to the tumble center position. The vectors represent the mean flow

From the correlation maps, it can be seen that there are adjacent positive and negative correlation regions near the tumble vortex at most crank angles, from the initial stage of the intake stroke to the end of the compression stroke, indicating that the cyclic variation of the tumble vortex position is the primary factor influencing the cyclic variation of the direction angle at the spark plug position at the ignition timing under the HTR condition. Meanwhile, some regions with flow separation and shear features also show high correlation coefficients, such as at 270 CAD, indicating that these flow characteristics are also one of the factors that induce the cyclic variation of the direction angle of flow at the spark plug position at the ignition timing.

In summary, the key factors that induce the cyclic variation of direction angle at the spark plug position at the ignition time under the LTR and HTR conditions are different. The former is mostly connected to the collision region of the two intake jet flows in the later stage of the intake stroke, whereas the latter is primarily related to the cyclic variation of the tumble vortex position. The way the fresh air enters the cylinder can be effectively controlled by opening or closing the intake flap, which in turn affects the global flow pattern within the cylinder. Compared with an open flap, closing the flap can effectively suppress the collision of the two intake jet flows, where the collision region is strongly unsteady. Instead, an organized large-scale tumble motion can be established earlier in the cylinder. Although closing the flap will introduce the cyclic variation of the tumble vortex

position, its influence on the cyclic variation of direction angle at the spark plug position at the ignition time is smaller than that of the collision of two intake jets under the LTR condition.

4.5 Distribution of Spatially Averaged Kinetic Energy (KE) and Turbulent Kinetic Energy (TKE)

In the previous sections, the cyclic variation of the direction angle of flow and its influencing factors at the spark plug position at the ignition time under two different intake conditions were analyzed in detail. The results show that the cyclic variation can be effectively reduced by closing the tumble flap. To further understand the flow characteristics near the spark plug position under the two working conditions, the evolution of the spatially averaged kinetic energy and turbulent kinetic energy within the field of view 1 during the compression stroke was calculated, as shown in Fig. 11.

The spatially averaged kinetic energy KE is defined by

$$KE = \frac{1}{IJ} \sum_{i=1}^{I} \sum_{j=1}^{J} \frac{1}{2} (\overline{u}_{ij}^2 + \overline{v}_{ij}^2) \tag{13}$$

where I and J are the numbers of horizontal and vertical cells, $\overline{u}_{ij}$ and $\overline{v}_{ij}$ are the ensemble-averaged velocity components of the cell (i, j) in the horizontal and vertical direction, respectively.

The spatially averaged turbulent kinetic energy TKE is defined by

$$TKE = \frac{1}{IJ} \sum_{i=1}^{I} \sum_{j=1}^{J} \frac{1}{2} ((u'_{ij})^2 + (v'_{ij})^2) \tag{14}$$

where u'_{ij} and v'_{ij} are the fluctuating part of the horizontal and vertical velocity. These fluctuations are the sum of turbulent fluctuations and cycle variations.

From the perspective of the overall distribution, closing the tumble flap can significantly increase the averaged kinetic energy and turbulent kinetic energy of the flow field near the spark plug position. As the piston begins to move upward at the beginning of the compression stroke, the intake valves are closing completely and the intake jet flows also fade away. At this stage, the large-scale tumble motion has not yet formed in the cylinder under the LTR condition, resulting in a gradual decrease in the averaged kinetic energy. Until around 240 CAD, a large-scale weak tumble flow began to develop, as shown in Fig. 7. However, the tumble motion has minimal impact on the flow near the spark plug because the tumble vortex was located in the middle and lower part of the cylinder. As the piston continues upward, the influence of the tumble motion progressively arises after 270 CAD, and the averaged kinetic energy also increases gradually. Under the HTR condition, since a large-scale strong tumble flow has formed in the cylinder in the early stage of intake, the averaged kinetic energy presents an increase under the combined influence of the tumble flow and the intake jet in the early stage of compression, and a local peak appears at 210 CAD. Then the average kinetic energy decreases slightly with the weakening of the influence of the intake jet until it disappears. In the middle stage of the compression stroke, with the continuous decrease of the cylinder volume and the increase of the piston speed, the tumble vortex gradually shifts upward and the strength of the tumble motion increases. As a result, the influence
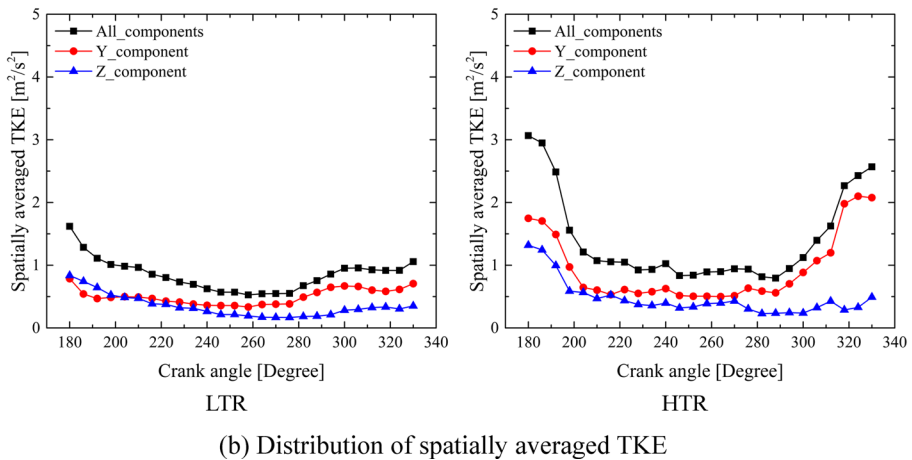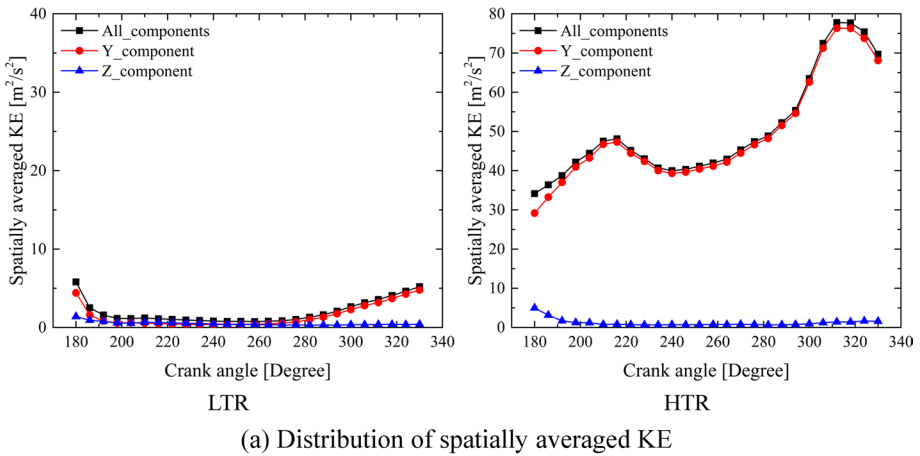
(a) Distribution of spatially averaged KE

(b) Distribution of spatially averaged TKE

Fig. 11 Evolution of spatially averaged **a** KE and **b** TKE within the field of view 1 under the LTR and HTR conditions

of the tumble motion on the flow field near the spark plug was enhanced, and the averaged kinetic energy keeps an increasing trend and reaches a maximum of around 310 CAD. Subsequently, in the late stage of the compression stroke, the piston speed gradually decreases, and the further reduction of the cylinder volume forces the tumble scale to be compressed in the longitudinal direction, resulting in a weakening of the tumble motion and a fall in averaged kinetic energy. For both two operating conditions, the horizontal velocity component contributes the most to averaged kinetic energy, while the contribution of the vertical velocity component was almost negligible. This finding is consistent with previous results unveiling the importance of the horizontal velocity component of in-cylinder flows in predicting engine performance (Dreher et al. 2021).

Under the influence of the weakening or disappearance of the intake jet, the averaged turbulent kinetic energy under the two conditions at the beginning of the compression stroke gradually decreases, and the contributions of the horizontal (Y) and vertical (Z)

components to the average turbulent kinetic energy are relatively close. In the middle and late stages of the compression stroke, the average turbulent kinetic energy increases gradually due to the tumble motion, and the horizontal (Y) component contributes significantly to the average turbulent kinetic energy. Besides, it can be clearly observed that the turbulent kinetic energy of the HTR condition in the late stage of the compression stroke is higher than that under the LTR condition.

5 Conclusions

In this study, experimental investigations on the CCV of the in-cylinder flow fields under two different tumble intensities generated by controlling a tumble flap open or closed were conducted in an optically accessible single-cylinder, SI engine by using high-speed PIV. Both the whole in-cylinder flow and the local flow in the vicinity of the spark plug are simultaneously captured at a constant engine speed of 800 rpm using two high-speed cameras in the measurements. To identify the influencing factors and differences of flow CCV at the spark plug position at the ignition timing under two operating conditions, a correlation map analysis was employed to build the relationship between the flow at the plug position and the flow distribution in the intake and compression stroke in time and space. The POD method was used first to extract the large-scale coherent structures and then reconstruct the flow fields to enhance the correlation between the above two. The flow characteristics combined with correlation map analysis under two operating conditions were described, respectively. Finally, the evolution of spatially averaged kinetic energy (KE) and turbulent kinetic energy (TKE) near the spark plug position during the compression stroke was analyzed. The major conclusions are summarized as follows:

1. The CCV component of the in-cylinder instantaneous flow fields can be effectively extracted by using the POD decomposition method, and the large-scale coherent structure can be contained in the reconstructed velocity field.
2. The position of the tumble flap significantly influences the in-cylinder flow structures and the flow characteristics at the spark plug position at the ignition timing. Compared with the LTR condition, the frequency distributions of the velocity magnitude and direction angle are more concentrated under the HTR condition, indicating that closing the tumble flap can effectively reduce the flow CCV at the spark plug position at the ignition timing.
3. The correlation map analysis revealed that the key factors influencing the CCV of flow direction at the ignition time at the spark plug position under the LTR and HTR conditions are different. The former is mostly attributed to the CCV of the collision region position of the two intake jet flows in the later stage of the intake stroke and flow shear with the combustion chamber wall at the late compression stroke, whereas the latter is primarily associated with the CCV of the tumble vortex position.
4. Compared with the LTR condition, the averaged kinetic energy and turbulent kinetic energy of the flow field close to the spark plug position can both be significantly increased by closing the tumble flap at the end of the compression stroke.

These experimental results will help researchers to further understand the physical processes of flow CCV in ICEs under different tumble intensities.

Declarations

Conflict of interest The authors declare that they have no conflict of interest.

References

Benoit, O., Truffin, K., Jay, S., van Oijen, J., Drouvin, Y., Kayashima, T., et al.: Development of a large-Eddy simulation methodology for the analysis of cycle-to-cycle combustion variability of a lean burn engine. Flow Turbul. Combust. **108**(2), 559–598 (2022). https://doi.org/10.1007/s10494-021-00278-7

Bode, J., Schorr, J., Krüger, C., Dreizler, A., Böhm, B.: Influence of three-dimensional in-cylinder flows on cycle-to-cycle variations in a fired stratified DISI engine measured by time-resolved dual-plane PIV. P. Combust. Inst. **36**(3), 3477–3485 (2017). https://doi.org/10.1016/j.proci.2016.07.106

Bücker, I., Karhoff, D.C., Klaas, M., Schröder, W.: Engine in-cylinder flow control via variable intake valve timing. SAE Technical Paper 2013-24-0055 (2013). https://doi.org/10.4271/2013-24-0055

Buschbeck, M., Bittner, N., Halfmann, T., Arndt, S.: Dependence of combustion dynamics in a gasoline engine upon the in-cylinder flow field, determined by high-speed PIV. Exp. Fluids **53**(6), 1701–1712 (2012). https://doi.org/10.1007/s00348-012-1384-3

Chu, H., Welch, C., Elmestikawy, H., Cao, S., Davidovic, M., Böhm, B., et al.: A combined numerical and experimental investigation of cycle-to-cycle variations in an optically accessible spark-ignition engine. Flow Turbul. Combust. (2022). https://doi.org/10.1007/s10494-022-00353-7

Dreher, D., Schmidt, M., Welch, C., Ourza, S., Zündorf, S., Maucher, J., et al.: Deep feature learning of in-cylinder flow fields to analyze cycle-to-cycle variations in an SI engine. Int. J. Engine Res. **22**(11), 3263–3285 (2021). https://doi.org/10.1177/1468087420974148

Freudenhammer, D., Peterson, B., Ding, C.P., Boehm, B., Grundmann, S.: The influence of cylinder head geometry variations on the volumetric intake flow captured by magnetic resonance velocimetry. SAE Technical Paper 2015-01-1697 (2015). https://doi.org/10.4271/2015-01-1697

Funk, C., Sick, V., Reuss, D.L., Dahm, W.J.: Turbulence properties of high and low swirl in-cylinder flows. SAE Paper 2002-01-2841 (2002). https://doi.org/10.4271/2002-01-2841

Gao, R., Shen, L., The, K.Y., Ge, P., Zhao, F., Hung, D.L.: Effects of outlier flow field on the characteristics of in-cylinder coherent structures identified by proper orthogonal decomposition-based conditional averaging and quadruple proper orthogonal decomposition. J. Eng. Gas Turb. Power (2019). https://doi.org/10.1115/1.4043307

Goryntsev, D., Sadiki, A., Klein, M., Janicka, J.: Large Eddy simulation based analysis of the effects of cycle-to-cycle variations on air–fuel mixing in realistic DISI IC-engines. P. Combust. Inst. **32**(2), 2759–2766 (2009). https://doi.org/10.1016/j.proci.2008.06.185

Granet, V., Vermorel, O., Lacour, C., Enaux, B., Dugué, V., Poinsot, T.: Large-Eddy simulation and experimental study of cycle-to-cycle variations of stable and unstable operating points in a spark ignition engine. Combust. Flame **159**(4), 1562–1575 (2012). https://doi.org/10.1016/j.combustflame.2011.11.018

Heywood, J.B.: Internal Combustion Engine Fundamentals Education. Combust Spark Ignition Engines **9**, 445–455 (2018)

Hinze, P.C., Cheng, W.K.: Assessing the factors affecting SI engine cycle-to-cycle variations at idle. Proc. Combust. Inst. **27**(2), 2119–2125 (1998). https://doi.org/10.1016/s0082-0784(98)80059-3

Holický, M.: Introduction to probability and statistics for engineers, 1st edn., pp. 142–144. Springer, Berlin (2013)

Jarvis, S., Justham, T., Clarke, A., Garner, C.P., Hargrave, G.K., Richardson, D.: Motored SI IC engine in-cylinder flow field measurement using time resolved digital PIV for characterisation of cyclic variation. SAE Technical Paper 2006-01-1044 (2006). https://doi.org/10.4271/2006-01-1044

Joo, S., Srinivasan, K., Lee, K., Bell, S.: The behaviour of small-and large-scale variations of in-cylinder flow during intake and compression strokes in a motored four-valve spark ignition engine. Int. J. Engine Res. **5**, 317–328 (2004). https://doi.org/10.1243/146808704323224222

Jung, D., Sasaki, K., Sugata, K., Matsuda, M., Yokomori, T., Iida, N.: Combined effects of spark discharge pattern and tumble level on cycle-to-cycle variations of combustion at lean limits of SI engine operation. SAE Technical Paper 2017-01-0677 (2017). https://doi.org/10.4271/2017-01-0677

Keane, R.D., Adrian, R.J.: Optimization of particle image velocimeters. Part I: double pulsed systems. Meas. Sci. Technol. **1**(11), 1202–1215 (1990). https://doi.org/10.1088/09570233/1/11/013

Laichter, J., Kaiser, S.A.: Optical investigation of the influence of in-cylinder flow and mixture inhomogeneity on cyclic variability in a direct-injection spark ignition engine. Flow Turbul. Combust. (2022). https://doi.org/10.1007/s10494-022-00344-8

Li, Y., Zhao, H., Leach, B., Ma, T., Ladommatos, N.: Characterization of an incylinder flow structure in a high-tumble SI engine. Int. J. Engine Res. **5**, 375–400 (2004). https://doi.org/10.1243/1468087042320924

Li, W., Li, Y., Wang, T., Jia, M., Che, Z., Liu, D.: Investigation of the effect of the in-cylinder tumble motion on cycle-to-cycle variations in a direct injection spark ignition (DISI) engine using large eddy simulation (LES). Flow. Turbul. Combust. **98**(2), 601–631 (2017). https://doi.org/10.1007/s10494-016-9773-y

Liu, D., Wang, T., Jia, M., Wang, G.: Cycle-to-cycle variation analysis of in-cylinder flow in a gasoline engine with variable valve lift. Exp. Fluids **53**(3), 585–602 (2012). https://doi.org/10.1007/s00348-012-1314-4

Liu, M., Zhao, F., Hung, D.L.: A coupled phase-invariant POD and DMD analysis for the characterization of in-cylinder cycle-to-cycle flow variations under different swirl conditions. Flow Turbul. Combust. (2022). https://doi.org/10.1007/s10494-022-00348-4

Lumley, J.L.: The structure of inhomogeneous turbulent flows. In: Atmospheric Turbulence and Radio Wave Propagation, Nauka, Moscow (1967)

Malé, Q., Staffelbach, G., Vermorel, O., Misdariis, A., Ravet, F., Poinsot, T.: Large eddy simulation of pre-chamber ignition in an internal combustion engine. Flow Turbul. Combust. **103**(2), 465–483 (2019). https://doi.org/10.1007/s10494-019-00026-y

Matsuda, M., Yokomori, T., Shimura, M., Minamoto, Y., Tanahashi, M., Iida, N.: Development of cycle-to-cycle variation of the tumble flow motion in a cylinder of a spark ignition internal combustion engine with Miller cycle. Int. J. Engine Res. **22**(5), 1512–1524 (2021). https://doi.org/10.1177/1468087420912136

Montgomery, D.C., Runger, G.C.: Applied Statistics and Probability for Engineers. Wiley, New York (2010)

Müller, S.H.R., Böhm, B., Gleißner, M., Grzeszik, R., Arndt, S., Dreizler, A.: Flow field measurements in an optically accessible, direct-injection spray-guided internal combustion engine using high-speed PIV. Exp. Fluids **48**(2), 281–290 (2010). https://doi.org/10.1007/s00348-009-0742-2

Okura, Y., Segawa, M., Onimaru, H., Urata, Y., Tanahashi, M.: Analysis of in-cylinder flow for a boosted GDI engine using high-speed particle image velocimetry. In: Proceedings of the 17th International Symposium on Applications of Laser Techniques to Fluid Mechanics, Lisbon, Portugal (2014)

Omura, T., Nakata, K., Yoshihara, Y., Takahashi, D.: Research on the measures for improving cycle-to-cycle variations under high tumble combustion. SAE Technical Paper 2016-01-0694 (2016). https://doi.org/10.4271/2016-01-0694

Ozdor, N., Dulger, M., Sher, E.: Cyclic Variability in Spark Ignition Engines: A Literature Survey. SAE Technical Paper 940987 (1994). https://doi.org/10.4271/940987

Pera, C., Knop, V., Chevillard, S., Reveillon, J.: Effects of residual burnt gas heterogeneity on cyclic variability in lean-burn SI engines. Flow Turbul. Combust. **92**(4), 837–863 (2014). https://doi.org/10.1007/s10494-014-9527-7

Qin, W., Xie, M., Jia, M., Wang, T., Liu, D.: Large eddy simulation and proper orthogonal decomposition analysis of turbulent flows in a direct injection spark ignition engine: cyclic variation and effect of valve lift. Sci. China Technol. Sc. **57**, 489–504 (2014). https://doi.org/10.1007/s11431-014-5472-x

Reuss, D.L.: Cyclic variability of large-scale turbulent structures in directed and undirected IC engine flows. SAE Technical Paper 2000-01-0246 (2000). https://doi.org/10.4271/2000-01-0246

Roudnitzky, S., Druault, P., Guibert, P.: Proper orthogonal decomposition of in-cylinder engine flow into mean component, coherent structures and random Gaussian fluctuations. J. Turbul. **7**, N70 (2006). https://doi.org/10.1080/14685240600806264

Rulli, F., Fontanesi, S., d'Adamo, A., Berni, F.: A critical review of flow field analysis methods involving proper orthogonal decomposition and quadruple proper orthogonal decomposition for internal combustion engines. Int. J. Engine Res. **22**(1), 222–242 (2021). https://doi.org/10.1177/14680 87419836178

Sirovich, L.: Chaotic dynamics of coherent structures. Phys. D **37**(1), 126–145 (1989). https://doi.org/10.1016/0167-2789(89)90123-1

Stiehl, R., Bode, J., Schorr, J., Krüger, C., Dreizler, A., Böhm, B.: Influence of intake geometry variations on in-cylinder flow and flow–spray interactions in a stratified direct-injection spark-ignition engine captured by time-resolved particle image velocimetry. Int. J. Engine Res. **17**(9), 983–997 (2016). https://doi.org/10.1177/1468087416633541

Towers, D.P., Towers, C.E.: Cyclic variability measurements of in-cylinder engine flows using high-speed particle image velocimetry. Meas. Sci. Technol. **15**(9), 1917–1925 (2004). https://doi.org/10.1088/0957-0233/15/9/032

Vu, T.T., Guibert, P.: Proper orthogonal decomposition analysis for cycle-to-cycle variations of engine flow. Effect of a control device in an inlet pipe. Exp. Fluids **52**(6), 1519–1532 (2012). https://doi.org/10.1007/s00348-012-1268-6

Wang, T., Li, W., Jia, M., Liu, D., Qin, W., Zhang, X.: Large-eddy simulation of in-cylinder flow in a DISI engine with charge motion control valve: proper orthogonal decomposition analysis and cyclic variation. Appl. Therm. Eng. **75**, 561–574 (2015). https://doi.org/10.1016/j.applthermaleng.2014.10.081

Wang, Y., Hung, D.L.S., Zhuang, H., Xu, M.: Cycle-to-cycle analysis of swirl flow fields inside a spark-ignition direct-injection engine cylinder using high-speed time-resolved particle image velocimetry. SAE Technical Paper 2016-01-0637 (2016). https://doi.org/10.4271/2016-01-0637

Welch, C., Schmidt, M., Illmann, L., Dreizler, A., Böhm, B.: The influence of flow on cycle-to-cycle variations in a spark-ignition engine: a parametric investigation of increasing exhaust gas recirculation levels. Flow Turbul. Combust. (2022). https://doi.org/10.1007/s10494-022-00347-5

Wu, S., Patel, S., Ameen, M.: Investigation of cycle-to-cycle variations in internal combustion engine using proper orthogonal decomposition. Flow Turbul. Combust. (2022). https://doi.org/10.1007/s10494-022-00368-0

Yin, C., Zhang, Z., Sun, Y., Sun, T., Zhang, R.: Effect of the piston top contour on the tumble flow and combustion features of a GDI engine with a CMCV: a CFD study. Eng. Appl. Comp. Fluid. **10**(1), 311–329 (2016). https://doi.org/10.1080/19942060.2016.1157099

Young, M.B.: Cyclic Dispersion in the Homogeneous-charge Spark-ignition Engine-a Literature Survey. SAE Technical Paper 810020 (1981). https://doi.org/10.4271/810020

Zhang, X., Wang, T., Jia, M., Li, W., Cui, L., Zhang, X.: The interactions of in-cylinder flow and fuel spray in a gasoline direct injection engine with variable tumble. J. Eng. Gas Turb. Power **137**(7), 071507 (2015). https://doi.org/10.1115/1.4029208

Authors and Affiliations

Fuquan Tian[1] · **Lei Shi**[1] · **Zhizhao Che**[1] · **Zhen Lu**[1] · **Kai Sun**[1] · **Tianyou Wang**[1]

✉ Tianyou Wang
    wangtianyou@tju.edu.cn

[1]   State Key Laboratory of Engines, Tianjin University, No. 92 Weijin Road, Nankai District, Tianjin, China